



## Offline tuning mechanism of joint angular controller for lower-limb exoskeleton with adaptive biogeographical-based optimization

Mohammad Soleimani Amiri<sup>1</sup> , Rizauddin Ramli<sup>1,2,\*</sup> 

<sup>1</sup>Department of Mechanical and Manufacturing Engineering, Faculty of Engineering and Built Environment, The National University of Malaysia, Malaysia

<sup>2</sup>Center for Automotive Research, Faculty of Engineering and Built Environment, The National University of Malaysia, Malaysia

Received: 01.11.2021

Accepted/Published Online: 12.04.2022

Final Version: 31.05.2022

**Abstract:** Designing an accurate controller to overcome the nonlinearity of dynamic systems is a technical matter in control engineering, particularly for tuning the parameters of the controller precisely. In this paper, a tuning mechanism for a proportional-integral-derivative (PID) controller of lower limb exoskeleton (LLE) joints by adaptive biogeographical based-optimization (ABBO) is presented. The tuning of the controller is defined as an optimization problem and solved by ABBO, which is an iterative algorithm inspired by a blending crossover operator (BLX- $\alpha$ ). The parameters of the migration change proportionally to the growth of iteration that conveys the error to rapid convergence by narrowing the searching space. The Lyapunov stability theory is proven for LLE nonlinear dynamic systems. ABBO algorithm is compared with other conventional optimization methods in step response, which guaranteed it was not trapped in local optima and demonstrated the lowest average error and the fastest convergence rate. The tuned controller is applied in a closed-loop system to verify its performance in the prototype. The experimental results of ABBO with PID controller ascertained that the proposed tuning mechanism is applicable in the LLE gait training.

**Key words:** Biogeographical-based optimization, proportional-integral-derivative controller, lower limb exoskeleton, trajectory control

### 1. Introduction

Currently, the rehabilitation process of the lower limb is challenging because it is labor-intensive and it highly relies on the skill of physiotherapists. The exoskeleton is a wearable robot that is used to increase human strength and stamina for rehabilitation and power enhancement for different tasks such as lifting heavy objects or standing a long time [1, 2]. In rehabilitation for disabled people who are struggling with mobility issues caused by stroke, spinal cord injuries, and aging, lower limb exoskeleton (LLE) has been utilized in providing gait assistance and a fast recovering process [3–5]. In addition, LLE releases physical stress of physiotherapists for gait training as rehabilitation devices [6–8].

The challenges of dealing with the control of the exoskeleton result from its complicated structure, which makes it difficult for wearers to use it during long rehabilitation processes. Furthermore, the control system should cope with various ranges of wearer's weight, size, and disability level. Therefore, selection of robust control methods for joint movement is essential in the development of rehabilitation LLE. Various control approaches have been carried out for LLE specialized in rehabilitation [9, 10].

\*Correspondence: rizauddin@ukm.edu.my

Developing control strategies in rehabilitation robots plays a important role in achieving satisfactory performance for various rehabilitation treatments [11]. However, due to the complexity of its dynamic plant with unknown uncertainties and variations, the development of a classical control system for LLE has been hindered. Therefore, the classical control system is usually combined with other techniques. For instance, He et al. [12] established a neural network (NN) feedback control system for a two-degree of freedom (DoF) knee rehabilitation robot with unknown parameters to overcome the disturbance and gain robustness of the control system. Shan et al. [13] applied a fuzzy logic controller and proportional-integral-derivative (FLC-PID) for a wearable one-DoF orthosis with active knee joint for walking assistance to reduce consumption of muscular power during gait training. Zhang et al. [14] classified the control part of the lower limb rehabilitation robot into stand and swing phases. They analyzed the kinetic model for both phases and employed sliding mode and fuzzy compensation method to reduce the disturbances in swing phase. Meanwhile, the cerebellar model articulation and proportional-integral-derivative (PID) controller for stand and swing phases have been established for stabilizing the control system. In addition, the stability validation of the proposed classified control method for a simulated model has been developed by Lyapunov stability theory. In a similar study, Li et al. [15] used a hybrid phase based on stand and swing phases of gait training to determine dynamic equations by Lagrangian and established their control system by a combination of the fuzzy and sliding mode controller. Even though there is a lot of research on the control of lower limb exoskeleton, most of the control techniques of rehabilitation robots required a treadmill, or at least one physiotherapist is needed when training. They manifest good performance of gait rehabilitation, but they are not suitable for a multiple-joint training application and they are complicated and high-cost. Hence, it is important to develop an affordable LLE with a high-accuracy control system by combining nonconventional optimization techniques with a simple classical control system such as PID.

In this paper, an adaptive biogeographical-based optimization (ABBO) with proportional migration operator parameter is presented. Different from other population-based methods, in biogeographical-based optimization (BBO), the qualities of bad solutions can be improved by accepting new features from good ones due to the ability to generate competitive candidates compared with other metaheuristic algorithms. BBO was introduced by Simon [16] as a novel optimization algorithm inspired by the natural biogeographical phenomenon, which has been used in many similar problems that other algorithms such as genetic algorithm (GA), particle swarm optimization (PSO), and ant colony optimization (ACO) are applicable [17, 18]. However, the uniqueness of BBO is in its migration operator, which is used for generating the new population from previous populations, and the mutation operator that employs a diversity of the possible solutions. Many types of research have been accomplished to increase its performance by modification of its operators. For instance, Wen et al. [19] analyzed the characteristics of global topology and direct-copying migration strategy to increase the convergence speed and accuracy and avoid homogenization of habitats in comparison with conventional BBO. In another work, to deal with reliability redundancy allocation problems of four various case studies such as series, series-parallel, bridge, and over-speed protection systems, Garg [20] presented an effective penalty-guided BBO algorithm for dealing with constraints and penalizing the infeasible solution. On the other hand, Reihanian et al. [21] developed an algorithm of BBO with two-phase migration operator to provide a balance between exploration and exploitation to decrease the chance of trapping in local optima. Statistical validation showed the superiority of their proposed algorithm to the other evolutionary algorithms.

For increasing the accuracy and robustness of the classical control system, one of the techniques is to combine it with optimization methods. So far various techniques of the optimized-based controller have

been designed by previous researchers. For instance, Misaghi et al. [22] utilized an improved invasive weed optimization algorithm to set the parameters of a PID controller for a DC motor. They defined the operators of the optimization algorithm to select a large value in focusing on more exploration at the beginning of the process. In the end, after approaching the neighbor of global optima, the searching space has been narrowed. Thus, exploration and exploitation were balanced. Pal et al. [23] employed PSO to design robust stable quadratic-optimal fuzzy controllers to achieve both robust stability and desired transient response. Their proposed method has better performance than the hybrid Taguchi genetic algorithm-based approach by achieving robust stability and desired transient response. Wang et al. [24] presented an optimal adaptive control scheme for nonlinear systems with input time-delays by using the online policy iteration algorithm. They validated their results on two simulations nonlinear examples. Therefore, although these are optimized-based controllers for the implementation of adaptive algorithms, we need to eliminate the external disturbances, which represent influences of interaction with human users during optimization process. Table 1 illustrates a literature analysis on the methods used in the design and control of LLE.

**Table 1.** Literature analysis of LLE control methods.

No.	Reference	Year	DoF	Controller type
1	[11]	2018	2	NN
2	[25]	2018	12	Adaptive PI
3	[26]	2021	8	Adaptive Lyapunov-based
4	[15]	2018	6	Fuzzy sliding mode
5	[27]	2021	2	Reduced adaptive fuzzy
6	[12]	2015	2	Adaptive controller
7	[13]	2016	1	FLC-PID
8	[15]	2018	6	Fuzzy sliding mode
9	[28]	2017	2	PSO-PID
10	[29]	2021	4	Dragon fly algorithm (DFA) and FLC-PID

In summary, the contributions of the paper are,

- An optimal PID controller for LLE rehabilitation application is presented;
- The stability of the control scheme is proven by Lyapunov approach;
- The applicability of the proposed optimization technique to minimize the steady-state trajectory error is investigated and compared with conventional optimization approaches;
- The validated results in the LLE prototype reveal efficiency of the proposed method.

The rest of the paper is structured as follows. In the beginning, the dynamic model of the LLE based on its structure is determined. The simulated model is used in a closed-loop control system with a PID controller. In the control system, ABBO is employed to tune the parameters of the PID controller by minimizing the root mean square error. Furthermore, the equation of the migration operator and its algorithm, which is an adaptation of the BBO, is explained. The performance of ABBO is compared with those of other conventional BBO algorithms. The stability of the nonlinear dynamic system of LLE is proved by the Lyapunov function. Finally, the tuned optimized control system is verified in a prototype of the LLE.

## 2. Dynamic model

In this paper, an LLE with a 4-DoF linkage that consists of two joints in each leg has been used. A 12V DC motor is employed and controlled by motor drivers to regulate its voltage and direction. A quadrature encoder is located at the connecting shaft to record the angle of each joint. An Arduino Mega 2560 is utilized to control the DC motor and capture the data from the encoder. Figure 1 illustrates the free body diagram of one leg of the LLE, length, and center of gravity (CoG) of each link joint.  $O_1$  and  $O_2$  are active hip and knee joints and  $O_3$  represents a passive ankle joint. Femur is from  $O_1$  to  $O_2$  and tibia is from  $O_2$  to the foot.

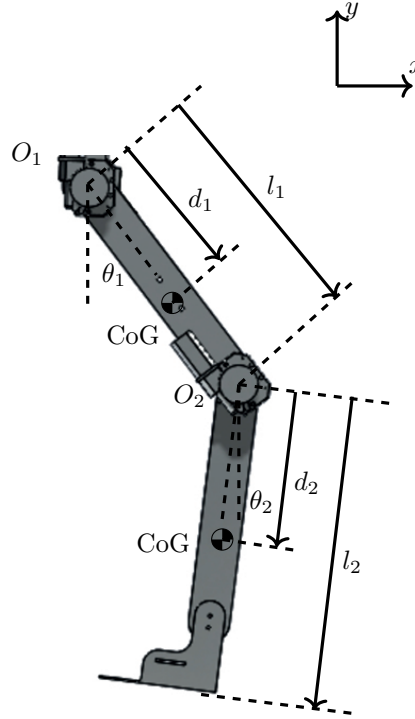


Figure 1. Free body diagram of the LLE.

The dynamic equation of LLE in state space is given as follows [31]:

$$\tau = M(\theta)\ddot{\theta} + V(\theta, \dot{\theta}) + G(\theta) \tag{1}$$

where  $\tau \in \mathbb{R}^4$  is torque vector,  $\ddot{\theta} \in \mathbb{R}^4$  denotes angular acceleration vector,  $M(\theta) \in \mathbb{R}^4$  is inertia and mass matrix,  $V(\dot{\theta}, \theta) \in \mathbb{R}^4$  represents vector of centrifugal and Coriolis vector, and  $G(\theta) \in \mathbb{R}^4$  introduces gravitational vector. In this paper, Lagrangian method has been applied to determine the dynamic equation as follows:

$$L = E_k - E_p \tag{2}$$

where  $E_k$  and  $E_p$  represent total kinematic and potential energy of the links, respectively. The following equations express the torque for hip and knee while  $j = 1, 2, 3, 4$  [32, 33].

$$\tau_j = \frac{d}{dt} \left( \frac{\partial L}{\partial \dot{\theta}_j} \right) - \left( \frac{\partial L}{\partial \theta_j} \right) + B\dot{\theta}_j \tag{3}$$

where  $B$  denotes the friction coefficient.  $\theta_j$  and  $\dot{\theta}_j$  are the angular trajectory and velocity of each link, respectively.  $E_k$  and  $E_p$  are expressed as follows:

$$E_p = \sum_{j=1}^4 m_j g y_j \quad (4)$$

$$E_k = \sum_{j=1}^4 \left[ \frac{1}{2} m_j (\dot{x}_j^2 + \dot{y}_j^2) + \frac{1}{2} I_j \dot{\theta}_j^2 \right] \quad (5)$$

where  $m_j$  and  $I_j$  are mass and inertia of the links.  $g$  is the gravity acceleration whereby  $x_i$  and  $y_i$  are the position of CoG for each link, respectively, given as follows:

$$x = \sum_{j=1}^{i-1} l_j \sin(\theta_j) + d_i \sin(\theta_i) \quad (6)$$

$$y = \sum_{j=1}^{i-1} -l_j \cos(\theta_j) - d_i \cos(\theta_i) \quad (7)$$

where  $l_j$  and  $d_i$  are length of each link and CoG, respectively. From mechanical structure in Figure 1, the torque applied to DC motor is represented as follows,

$$\tau_j = K_g \tau_m \quad (8)$$

where  $K_g$  is the gear ratio.

### 3. Motor model

The torque applied to each joint is provided by a DC motor which turns electrical to mechanical energy [34]. From Kirchhoff's law, the DC motor can be expressed as follows:

$$U - U_b = L_k \left( \frac{di}{dt} \right) + RI \quad (9)$$

where  $L_k$  and  $R$  are motor coil inductance, and resistance;  $U$  and  $I$  are input voltage and current of the DC motor, respectively.  $U_b$  represents back electromotive force voltage, which occurs due to a change in current across the coil of the DC motor and causes a change in the magnetic field and therefore produces a self-induced voltage [35, 36] as follows:

$$U_b = K_c \dot{\theta} \quad (10)$$

where  $K_c$  is the voltage constant and  $\dot{\theta}$  is angular velocity of the rotor shaft of the DC motor. The torque produced is expressed as follows:

$$\tau_m = K_m I \quad (11)$$

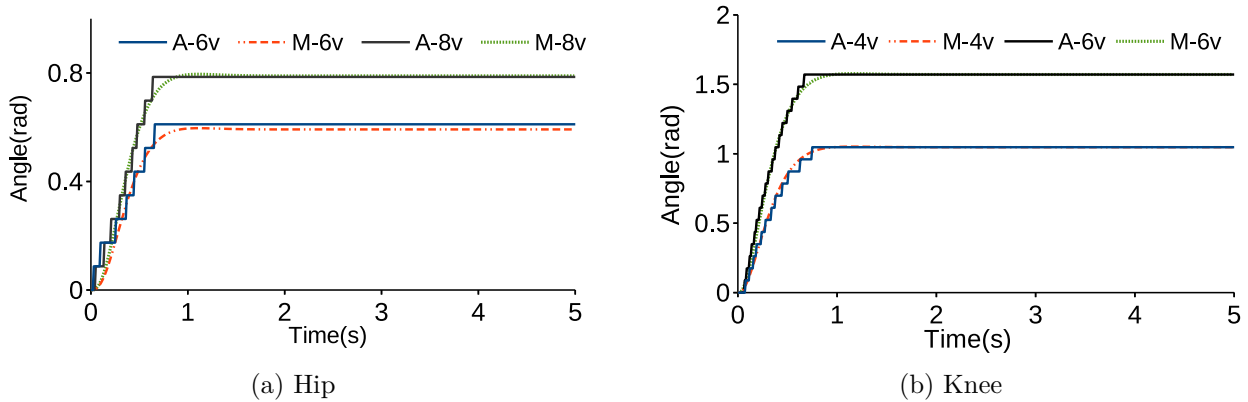
where  $K_m$  is the torque sensitivity. Table 2 represents the parameters of physical features of the LLE [37].

Since the LLE has symmetric parallel legs, in Table 2 we consider physical features for one leg.

**Table 2.** Parameters of physical features.

Parameters	j=1	j=2
$m_j(kg)$	0.387	0.4
$l_j(m)$	0.41	0.43
$d_j(m)$	0.2	0.21
$I_j(kg \cdot m^2)$	0.0055	0.0064
$K_m(Nm/A)$	1.92	1.92
$R(\Omega)$	3.7	3.7
$L(H)$	1.3720	1.3720
$K_c(V/rad.s^{-1})$	0.016	0.016
$K_g$	8	8
$B$	0.035	0.035
$\tau_{max}(Nm)$	9.6	9.6

$\tau_{max}$  denotes maximum torque of the DC motor. By using the parameters of Table 2, a simulation model to verify its response has been conducted as in Figure 2, in which the actual angular trajectory is captured by the encoder of the LLE. Various inputs of the hip are set as 6V and 8V for validation purpose. Similarly, knee 4V and 6V are applied as the step response in an open-loop.

**Figure 2.** Validation of angular trajectory in open-loop.

In Figure 2, A- and M- are the angular trajectories for actual and simulation of each joint. For instance, in Figure 2b, A-4v and M-4v are the angular trajectories while the 4v is applied to actual and simulation of knee, respectively. Figure 3 represents the error between actual and simulation for hip and knee. Figure 4 shows the torque applied to hip and knee by actuators. As can be seen it does not exceed the  $\tau_{max}(Nm)$  which is 9.6 (Nm). Figure 5 illustrates the angular velocity for hip and knee for actual trajectories.

A statistical analysis is expressed in Table 3, in which ME, AE, and RSME represent maximum error, average error, and root mean square error of the angular trajectory, respectively. The units of the errors are measured in the radian.

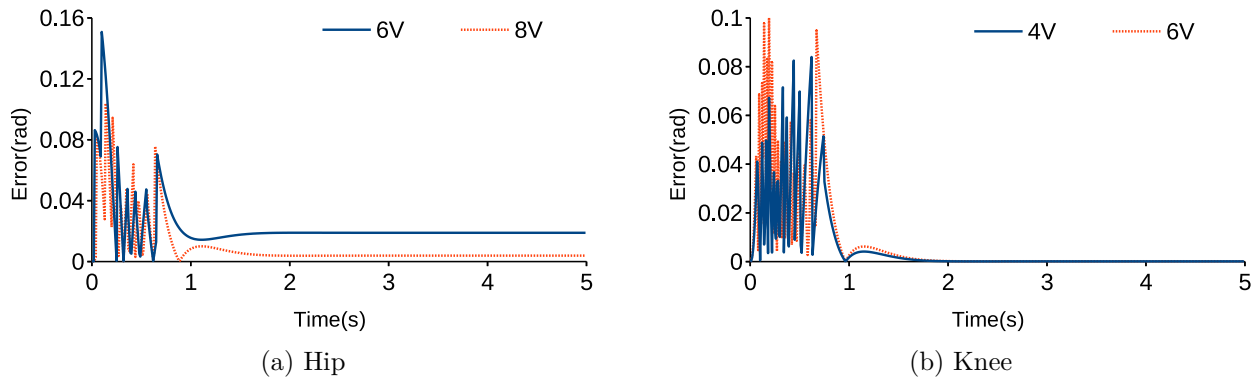


**Figure 3.** Trajectory error between actual and simulation for hip and knee.

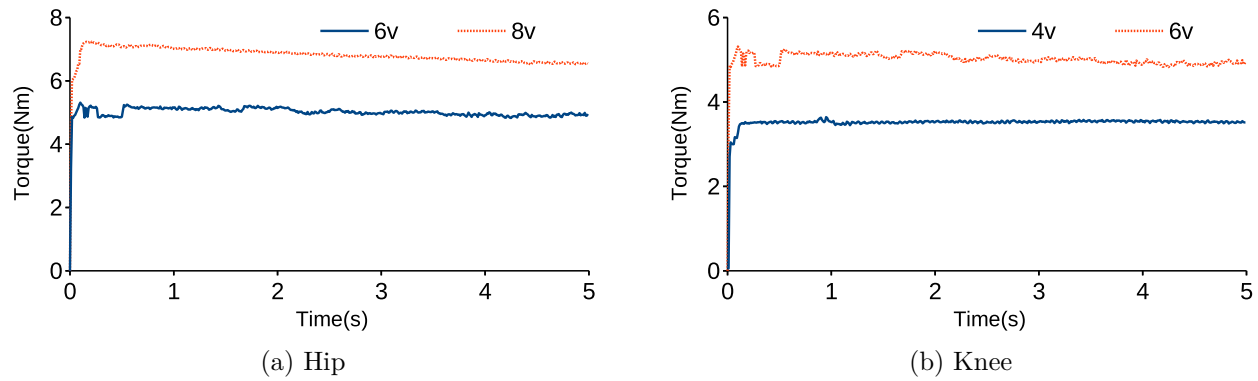


**Figure 4.** Torque applied to actuators of hip and knee.

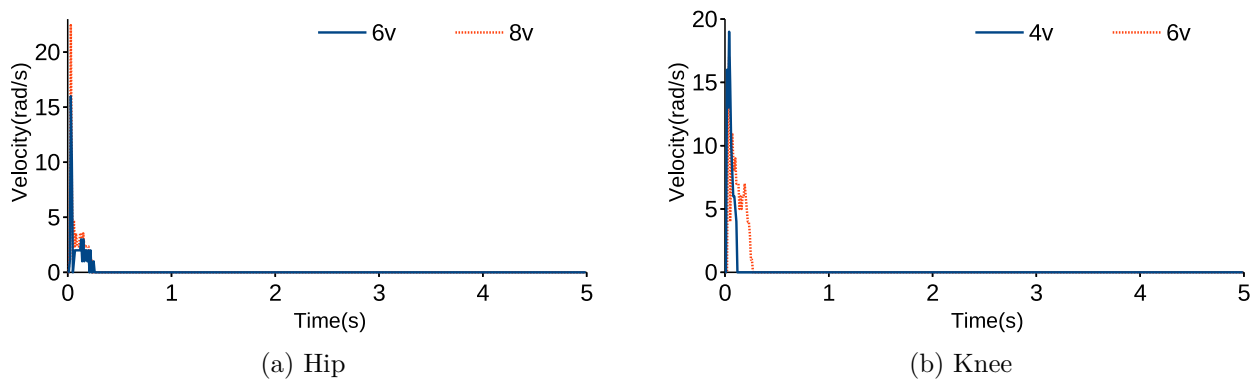


**Figure 5.** Angular velocity of hip and knee.

#### 4. Development of control strategy

In this paper, a tuning mechanism for a PID-based controller with ABBO algorithm is used to control LLE joints' position in offline mode. PID has been regarded as one of the most popular controllers in the industry because of its ease of implementation, and efficient performance [38, 39]. The controller has a first-order transfer function in the derivative expression to maintain the stability in high-frequency noises that are produced by the

**Table 3.** Trajectory error for each joint in open-loop.

Hip				Knee			
Voltages	ME	AE	RSME	Voltages	ME	AE	RSME
6V	0.15	0.022	0.028	4V	0.083	0.005	0.0015
8V	0.10	0.009	0.018	6V	0.1	0.006	0.018

encoder [40]. The expression of the PID controller is given as follows,

$$C(s) = K_p + \frac{K_i}{s} + \frac{K_d s}{s + N} \tag{12}$$

where  $N$  is the parameter of the transfer function of filter for derivative part of PID controller.  $C(s)$  exhibits a filtered PID, which is demonstrated in Figure 6.

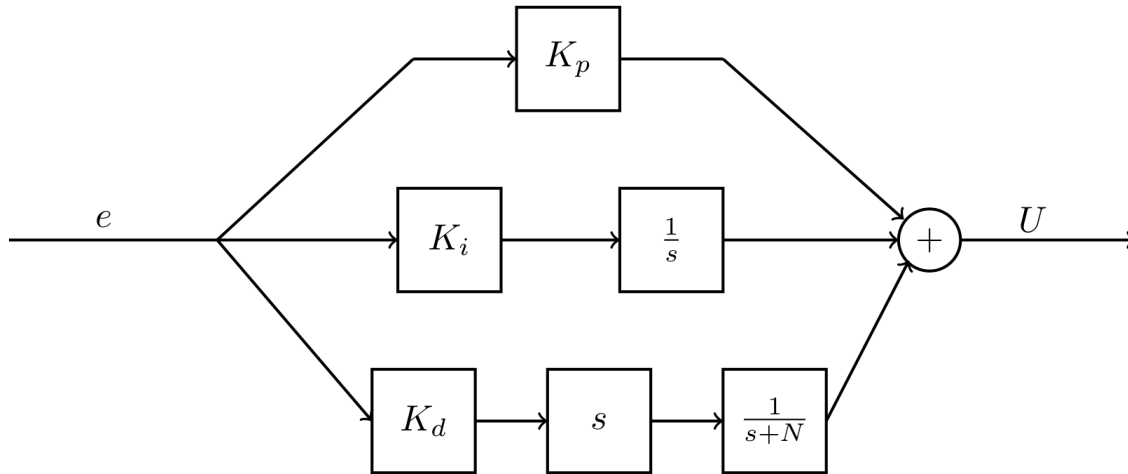


**Figure 6.** Filtered PID controller  $C(s)$ .

The gains of  $K_p$ ,  $K_i$ , and  $K_d$  represent proportional, integral, and derivative parameters of the controller, respectively. Input  $U$  is fed to the LLE plant, and  $e$  represents the steady-state error, that is the difference between actual and desired angular trajectories of hip and knee as:

$$e = \theta_d - \theta_a \tag{13}$$

where  $\theta_d$  and  $\theta_a$  are the desired and actual angular trajectories, respectively.

### 5. Optimal controller tuning

The PID controller is tuned as an optimization problem to minimize the RMSE of joints' trajectory. There are few functions for qualifying the cumulative summation of the error that can be used as an objective function such as integral absolute error (IAE) and integral time-weighted absolute error. In this paper, RMSE is utilized as an objective function, because it shows the calculated trajectory of each habitat spared out from the desired



input of the control system.

$$RMSE = \sqrt{\frac{\sum_{i=1}^n e_i^2}{n}} \tag{14}$$

where  $e_i \in \mathbb{R}^n$  is an error vector, represented in Equation 13. The design variables of the optimization problem are optimized so that the objective function can be minimized [41]. The initial population of ABBO is set randomly. Each population consists of habitats including the parameters of the filtered PID controller, given as follows:

$$x = [K_p \quad K_i \quad K_d \quad N] \tag{15}$$

where  $x$  represents a habitat of a population. The size of the population is usually selected based on the decision of the designer. Although some methods have been used for selecting the number of population in evolutionary algorithms such as Taguchi which is a kind of experimental design method [42, 43], population size is set as 40 based on trial-and-error. Subsequently, the habitat is evaluated by determining the objective function and sorted in ascending order. Twenty percent of the habitats remain unchanged as the elites. The rest of the habitats are changed by migration and mutation to keep the diversity which finally increases the chance for ABBO in finding global optima and avoiding trapping in the local ones. Figure 7 represents changes in emigration and immigration rate in one habitat.

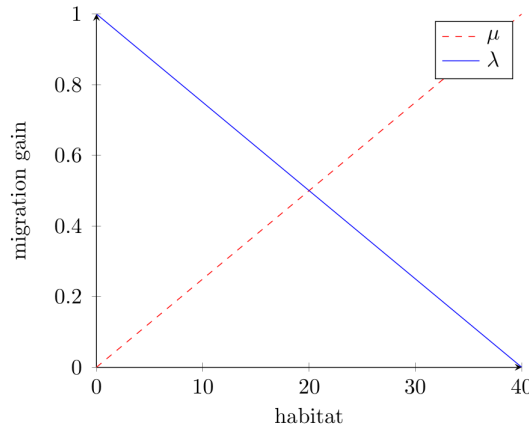


Figure 7. Changes in emigration and immigration rates.

In Figure 7,  $\lambda$  and  $\mu$  are immigration and emigration rates that are set for each individual of habitats. The first habitat has the lowest emigration and the highest immigration rate. Ironically, the rates of emigration and immigration are the highest and lowest in the last habitat, respectively. For applying the migration operator, a random value has been generated to be compared with  $\lambda$  of all the habitats. If the random number is less than the  $\lambda$ , the new habitats for the next iteration will be determined based on the migration operator which is inspired from blending crossover (BLX- $\alpha$ ) [44, 45]. The usage of blending crossover as a migration operator raises the convergence speed and the performance of the conventional BBO method. The migration operator is given as follows:

$$x_{i,j} = \omega((x_{k,j} + \alpha_1) - (x_{i-1,j} - \alpha_2)) \tag{16}$$

where  $i$  is the number of current habitats and  $j$  represents the iteration.  $\omega$ ,  $\alpha_1$ , and  $\alpha_2$  are the parameters of

the migration operator.  $k$  is selected by the roulette wheel scheme, which is based on emigration probabilities,

$$e_{p_i} = \frac{\mu_i}{\sum_{i=1}^{i_{max}} \mu_i} \quad for \quad i = 1 : i_{max} \quad (17)$$

where  $i_{max}$  is the total number of habitats. The cumulative summation of the  $e_p$  is given as:

$$C_i = \sum_{i=1}^{i_{max}} e_{p_i} \quad (18)$$

where  $C_i$  and  $e_{p_i}$  are  $1 \times i_{max}$  vectors. The roulette wheel scheme selects a random value and compares it with  $C_i$ . The number of the first element of  $C_i$  vector that is greater than the random value is selected as the  $k$ -th habitat. It provides more chances for the selection of the habitats with a higher rate of emigration. The parameters of the migration operator such as  $\omega$ ,  $\alpha_1$ , and  $\alpha_2$  are not constant during the iterations and are changed by increasing their number. This increases exploration of searching space at the beginning of the algorithm, and narrows to the global optima by increasing the number of iterations given as follows:

$$\omega = \omega_{int} b \quad (19)$$

$$\alpha_1 = 2.3b + 2.6 \quad (20)$$

$$\alpha_2 = 2.3a + 0.1 \quad (21)$$

where  $b$  and  $a$  are decreasing and increasing values between 0 and 1 as follows:

$$a = \frac{j}{j_{max}} \quad for \quad j = 1 : j_{max} \quad (22)$$

$$b = 1 - a \quad (23)$$

where  $j_{max}$  is the maximum value of the iteration. The value of  $\omega$  starts from 1.2 and decreases gradually. This provides the wide searching space for ABBO in the initial iterations and narrows the exploration for finding global optima at the end of the algorithm. In equations (20) and (21), the summation of  $\alpha_1$ , and  $\alpha_2$  is 5, while  $\alpha_1$  and  $\alpha_2$  are downward and upward entire iterations, respectively [39, 46]. Figure 8 exhibits how migration parameters modify by changing the number of iterations.

After applying the migration operator, the mutation is carried out to keep the diversity in ABBO. The mutation probability  $m_p$  is a positive number between zero and one.

$$m_p \in [0, 1] \quad (24)$$

The mutation operator is expressed as follows:

$$if \quad r < m_p : \quad x_{i,j} = x_{i-1,j} + \sigma \quad for \quad i = 1 : i_{max} \quad (25)$$

where  $r$  and  $\sigma$  are random values between 0 and 1. After establishing the migration and mutation operators, each habitat is evaluated by the objective function. All the habitats are sorted in descending order from the

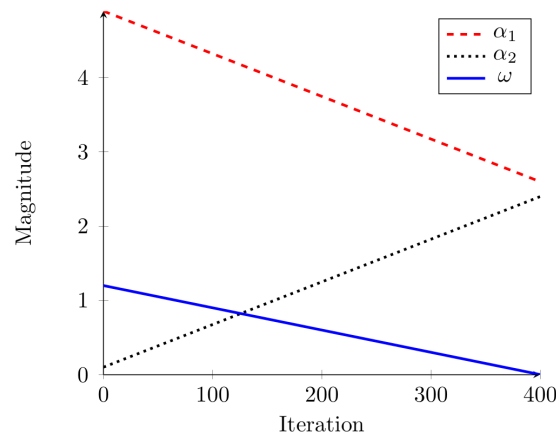


**Figure 8.** Changes of parameters of ABBO.

lowest to the highest quantity. Therefore, the first habitat is the output of the ABBO. Algorithm 1 exhibits the pseudocode and flow chart.

---

**Algorithm 1** Pseudocode of ABBO.

---

```

1: Start
2: Initialize 40 habitats randomly;
3: Set parameters for  $\mu$  and  $\lambda$ ;
4: while Number of  $i_{max} = 400$  do ;
5:   for j=1: $j_{max}$ 
6:     for i=1: $i_{max}$ 
7:       if  $r < \lambda_i$ 
8:         Calculate  $x_{i,j} = \omega((x_{k,j} + \alpha_1) - (x_{i-1,j} - \alpha_2))$ 
9:       end
10:    end
11:  end
12:  for i=1: $i_{max}$ 
13:    if  $r < m_p$ 
14:      Calculate  $x_{i,j} = x_{i-1,j} + \sigma$  for  $i = 1 : i_{max}$ 
15:    end
16:    Evaluate the habitats
17:    Sort the habitats
18: end while
19: Select the first habitat as a result
20: End;

```

---

In addition, a penalty function is set for each habitat, which contains the negative value equal to zero because parameters of filtered PID controller are defined as nonnegative values.

$$x_{i,j} = \max(x_{i,j}, 0) \quad (26)$$

Moreover, in order to simulate the actual conditions for the ABBO algorithm to tune the filtered PID controller, the high-frequency disturbance is implemented in the closed-loop control system for evaluation. The

simulated disturbance  $D(s)$  represents the high-frequency noises that are produced by the encoder in the actual LLE. Figure 9 shows the block diagram of the ABBO and filtered PID controller in the presence of the noises.

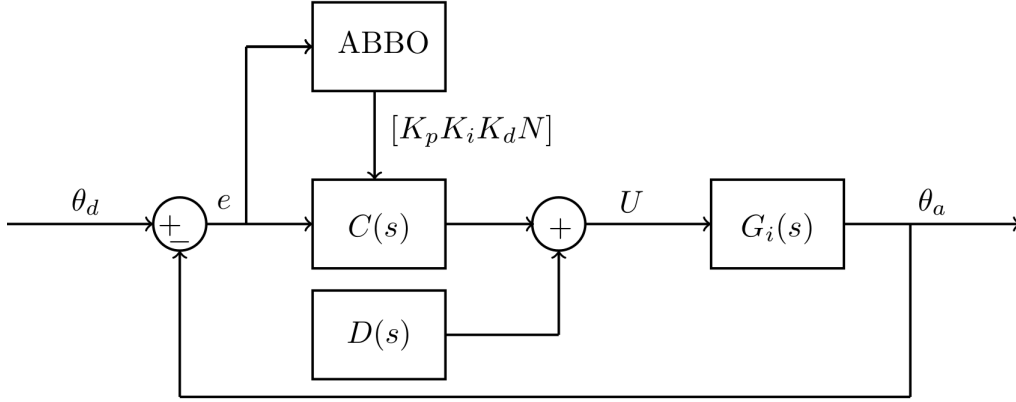


Figure 9. Block diagram of ABBO and closed-loop control system.

### 6. Stability analysis

**Theorem 1.** Consider a general nonlinear dynamic system

$$\dot{x} = f(x), \quad x \in \mathfrak{R}^n, \quad f(0) = 0 \tag{27}$$

where  $f : \mathfrak{R}^n \rightarrow \mathfrak{R}^n$  is a Lipschitz function. Consider a function  $V : \mathfrak{R}^n \rightarrow [0, \infty]$  which is positive definite and  $C^1$  with locally Lipschitz gradient, which is denoted by  $V_x$ . Lyapunov function for the nonlinear dynamic system exists by applying the following condition:

$$\dot{V} := V_x(x) \cdot f(x) < 0 \quad \forall x \neq 0 \tag{28}$$

The nonlinear dynamic system can be shown to be asymptotically stable if such a Lyapunov function exists [47–49]. In this paper, the closed-loop system of each joint is analyzed by Lyapunov stability theory. The transfer function of closed-loop control system is represented as follows:

$$G(s)_{cl} = \frac{\theta_a}{\theta_d} = \frac{G_i(s)C(s)}{1 + G_i(s)C(s)} \tag{29}$$

In the closed-loop control system,  $G_i(s)$  and  $C(s)$  are the is third- and second-order transfer functions, respectively. Therefore, closed-loop transfer function of the LLE is shown as follows:

$$G(s)_{cl} = \frac{a_2s^2 + a_1s^1 + a_0}{s^5 + b_4s^4 + b_3s^3 + b_2s^2 + b_1s^1 + b_0} \tag{30}$$

The steady-state of the control system is represented as follows:

$$\dot{X} = AX + Bu \tag{31}$$

$$y = CX + Du \quad (32)$$

The matrices  $A$ ,  $B$ ,  $C$ , and  $D$  are represented as follows:

$$A = \begin{bmatrix} -b_4 & -b_3 & -b_2 & -b_1 & -b_0 \\ 1 & 0 & 0 & 0 & 0 \\ 0 & 1 & 0 & 0 & 0 \\ 0 & 0 & 1 & 0 & 0 \\ 0 & 0 & 0 & 1 & 0 \end{bmatrix} \quad B = \begin{bmatrix} 1 \\ 0 \\ 0 \\ 0 \\ 0 \end{bmatrix} \quad (33)$$

$$C = [0 \quad 0 \quad a_2 \quad a_1 \quad a_0] \quad D = [0] \quad (34)$$

$u$  is the output of the PID and  $e$  is the error of the control system shown as follows:

$$e = r - y = r - CX \quad (35)$$

$y$  is the output of the plant. By defining  $O = [1 \quad \frac{1}{s} \quad \frac{s}{s+N}]$  and  $\theta = \begin{bmatrix} K_p \\ K_i \\ K_d \end{bmatrix}$ , the PID controller can be given as follows:

$$u = [1 \quad \frac{1}{s} \quad \frac{s}{s+N}] \begin{bmatrix} K_p \\ K_i \\ K_d \end{bmatrix} (r - CX) = O\theta(r - CX) \quad (36)$$

$r$  is the input of the control system. A Lyapunov function candidate is selected as  $V(x) = X^T P X$ , where  $P \in \mathbb{R}^{4 \times 4}$  is an identity matrix, which is positive definite; therefore,  $V$  is positive as well [50]. The derivative of the Lyapunov function is shown as follows:

$$\dot{V}(x) = X^T (A^T P + P A) X + B^T u P X + X^T P B u \quad (37)$$

By substituting Equation 36 into Equation 37, derivative of the Lyapunov function is written as the following equation,

$$\dot{V}(x) = X^T (A^T P + P A) X + B^T O \theta (r - CX) P X + X^T P B O \theta (r - CX) \quad (38)$$

By applying the optimization operator, the output of the control system  $y = CX$  will be equal to the input of the control system  $r$ , ( $r \approx CX$ ). Therefore, Equation 38 is written as follows:

$$\dot{V}(x) = X^T (A^T P + P A) X \quad (39)$$

where  $Q$  is substituted by  $A^T P + P A$ ,

$$\dot{V}(x) = X^T Q X \quad (40)$$

If  $P$  and  $Q$  become positive and negative definite, respectively,  $\dot{V}(x)$  and  $V(x)$  will be negative and positive definite. Therefore, the nonlinear dynamic system of LLE satisfies Theorem 1.

**Table 4.** Parameters used in GA, PSO, and ABBO.

Parameters	GA	PSO	ABBO
No. of iteration	400	400	400
No. of population	40	40	40
Objective function	RMSE	RMSE	RMSE
No. of design variables	4	4	4
Mutation probability	0.1	N/A	0.1
Crossover probability	0.1	N/A	N/A
Inertia parameter	N/A	1.2	N/A
Cognitive parameter	N/A	2	N/A
Social parameter	N/A	2	N/A

**7. Results and discussion**

In order to verify the performance of the proposed ABBO, the PID controller is tuned using GA and PSO for the hip and knee joints. Table 4 shows the parameters used in GA, PSO, and ABBO.

Figures 10 and 11 compare the step response and angular velocity of PID control system tuned by GA, PSO, and ABBO. Figure 12 shows torque of the step response for hip and knee.

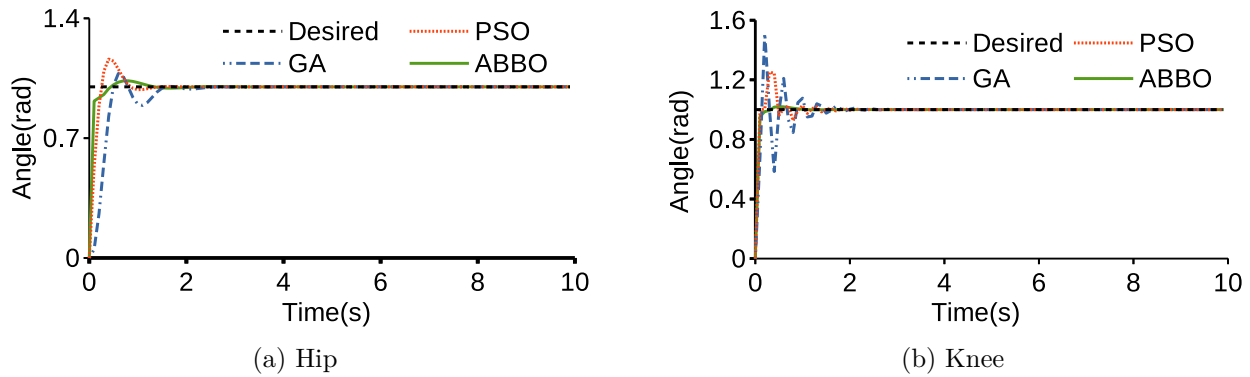


**Figure 10.** Step response tuned by GA, PSO, and ABBO.

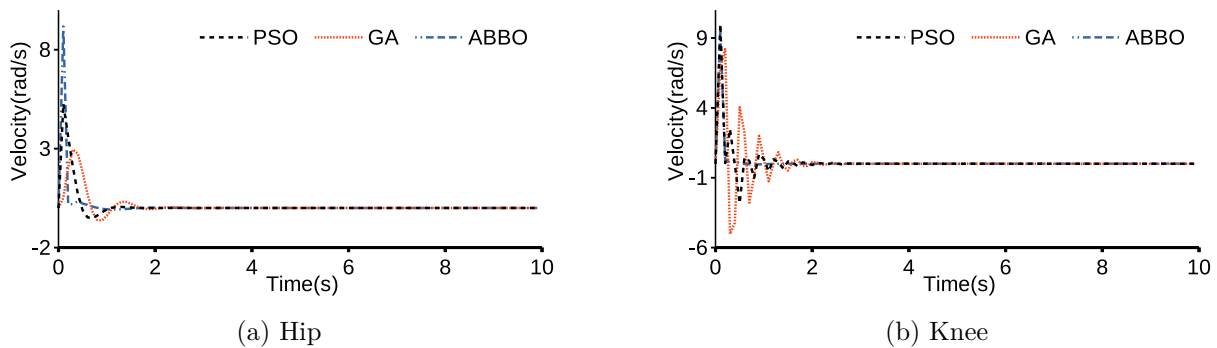


**Figure 11.** Angular velocity of step response tuned by GA, PSO, and ABBO.

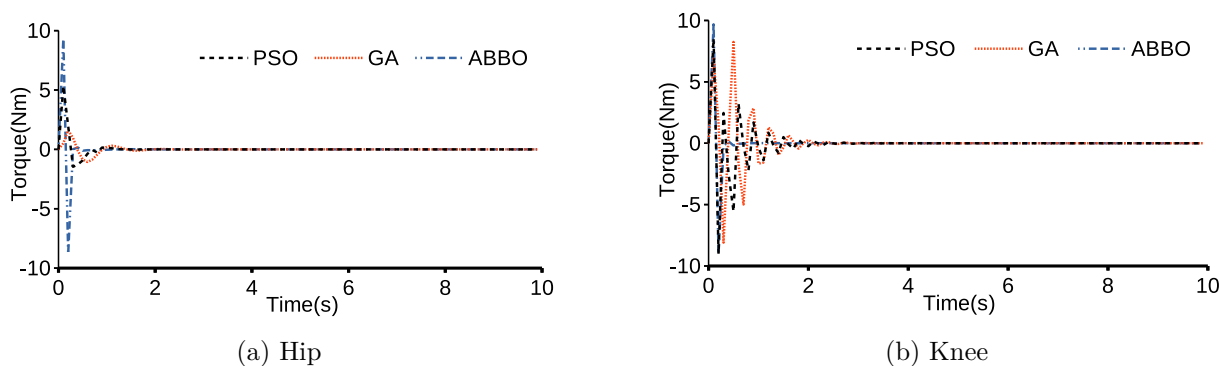


**Figure 12.** Torque of step response tuned by GA, PSO, and ABBO.

In Figure 12, the maximum torque applied is 8.2 Nm and 9.1 Nm for hip and knee, respectively, which are less than the  $\tau_{max}$ . Settling times of the GA, PSO, and ABBO for the hip are 1.6, 1.16, and 1 second, respectively. Similarly, the settling time for the knee is 1.5, 1.2, and 0.2 s. The AE for the hip is measured as 0.026, 0.022, 0.015 radian for GA, PSO, and ABBO, respectively. Similarly, the AE for the knee is calculated by 0.028, 0.018, 0.012 radians, respectively. These statistical data represent that ABBO performed better with the lowest average error and settling time than GA and PSO. Table 5 shows the statistical analysis for step responses of GA, PSO, and ABBO.

**Table 5.** Statistical analysis for step responses.

Methods	Hip			Knee		
	Settling time	Overshoot	AE	Settling time	Overshoot	AE
GA	1.6s	49.04	0.026rad	1.5s	14.86	0.028rad
PSO	1.16s	16.25	0.022rad	1.2s	25.06	0.018rad
ABBO	1s	4.3	0.015rad	0.2s	1.97	0.012rad

Overshoot for ABBO is the lowest. For instance, it is 91% and 73% less than PSO and GA. In the experimental test, two other types of BBO algorithms with different migration operators have been developed to compare the performance of tuning of PID ABBO. Table 6 expresses the equations of three different migration operators of the BBO that are used for tuning the controller. Constant values are used for migration operators of BBO-C and BBO-C- $\alpha$  that are inspired by arithmetic and  $BLX - \alpha$  crossovers, respectively. The condition of verification and mutation operator is similar in all algorithms.

**Table 6.** Different types of BBO algorithm.

Algorithm	Migration operator	$\alpha_1$	$\alpha_1$	$\omega$
BBO-C	$x_{i-1,j} + \alpha_1(x_{k,j} - x_{i-1,j})$	0.1	-	-
BBO-C- $\alpha$	$\omega((x_{k,j} + \alpha_1) - (x_{i-1,j} - \alpha_1))$	0.1	-	1.2
ABBO	$\omega((x_{k,j} + \alpha_1) - (x_{i-1,j} - \alpha_2))$	$2.3b + 2.6$	$2.3a + 0.1$	$1.2w$

To compare the performances of the different BBO algorithms given in Table 6, the three algorithms are applied to the closed-loop control system. The optimization algorithms are run ten different times. After

obtaining the results, the average errors of the control system for every ten sets of controller parameters are determined. In Table 7,  $AE_{BBO-C}$ ,  $AE_{BBO-C-\alpha}$ , and  $AE_{ABBO}$  are the average of ten various runs and  $p$ -value, which is determined by t-test of ANOVA, shows that diversity of the errors established by the three algorithms [51].

**Table 7.** Average error for BBO algorithms in radian.

Joints	$AE_{BBO-C}$	$AE_{BBO-C-\alpha}$	$AE_{ABBO}$	$P$ -value
Hip	0.0466	0.0438	0.0355	0.03297
Knee	0.0480	0.0382	0.0317	0.0384

The average errors for all the algorithms are less than 0.05 (rad), which is in the acceptable range [52], whereby the average error of trajectory error for ABBO is the lowest and BBO-C- $\alpha$  is lower than BBO-C. This shows that applying BLX- $\alpha$  as a migration operator improved the performance compared to the arithmetic migration operator; in addition, applying the adaptive variables instead of selecting constant values for BLX- $\alpha$  migration operator improved the algorithm efficiency because it provides a dynamic exploration mechanism for ABBO algorithm to find the global optima and not being trapped in the local ones. The  $P$ -value of the ANOVA test is less than 0.05, which expresses that the average error for ten times, running of algorithms is different from each other. Figure 13 represents the objective function that is in the first habitat as an elite, while the number of habitats is 40 and the three algorithms are run for 400 iterations.

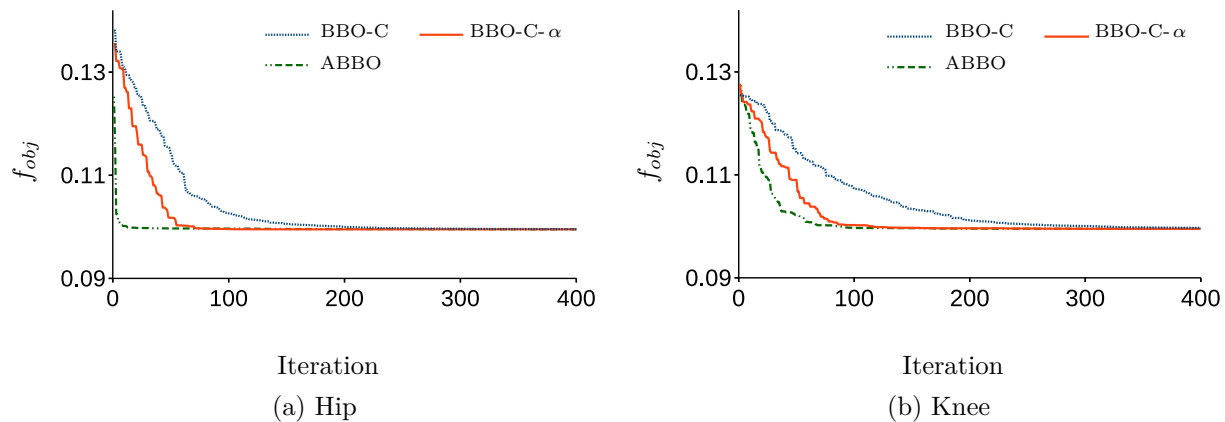


**Figure 13.** Objective function of each iteration.

For both hip and knee, ABBO has the fastest convergence, while BBO-C- $\alpha$  with BLX- $\alpha$  migration operator converges faster than BBO-C that uses arithmetic migration operator. Adaptive variables for BLX- $\alpha$  lead the algorithm to reach the neighbor of the global optimum in a few iterations and explore the global optimum in limited searching space throughout the iterations.

For instance, the objective function reached 80 percent of its optimal value in 13, 39, and 63 iterations for ABBO, BBO-C, and BBO for the hip. Similarly, knee algorithms achieved 80 percent of the final objective function in 33, 57, and 130 iterations for ABBO, BBO-C, and BBO, respectively. These data show that ABBO converges faster because the parameters of the migration operator change proportional to the number of iteration, and starts with a larger range of searching space and narrows it to the global optima. Table 8 shows



the parameters of optimal PID controller by ABBO with a transfer function as a filter on a derivative section of the controller to reduce high-frequency noises created by the encoder.

**Table 8.** Parameters of optimal filtered PID.

	$K_p$	$K_i$	$K_d$	$N$
Hip	0.633	3.8251	6.9418	38.6768
Knee	0.3141	1.3625	2.7641	68.1906

To validate the performance of ABBO in an experimental platform, the closed-loop control system with the optimal controller by parameters in Table 8 is implemented in a real prototype of the LLE. The desired trajectory for hip and knee is a periodic trajectory that has a stand and swing phases of the gait training. Figure 14 shows the angular trajectory for hip and knee joints. The desired trajectories, determined for the rehabilitation gait training exercise, are inspired by the stand and swing phases of healthy human walking [11]. The desired trajectory equations for left hip, left knee, right hip, and right knee are expressed as follows:

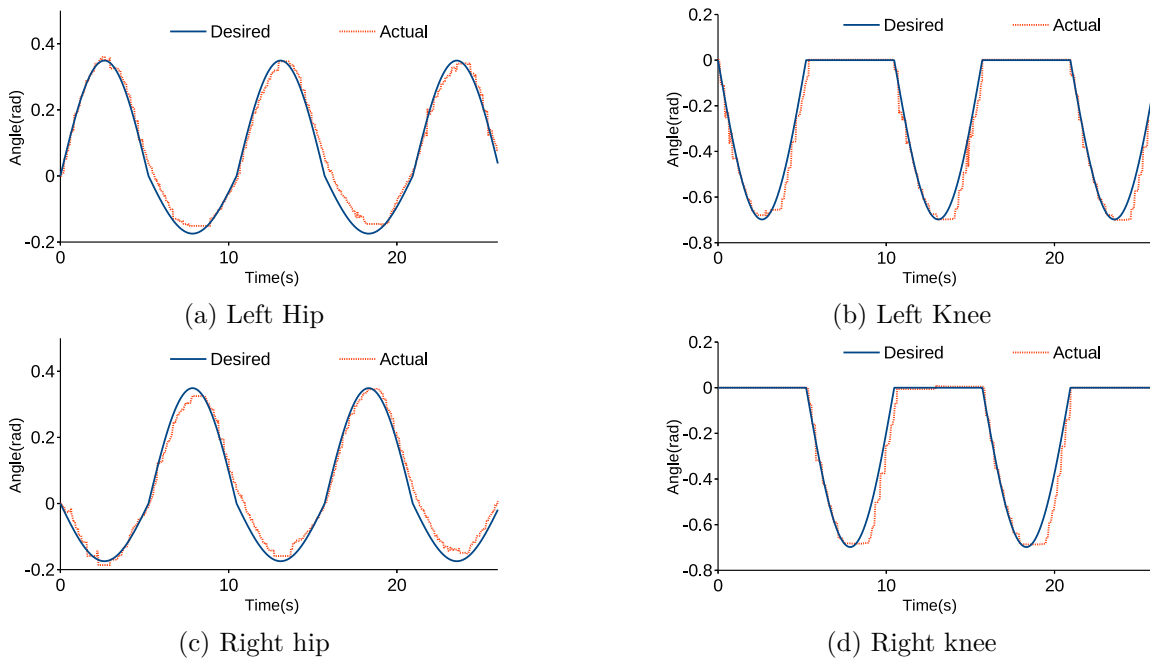
$$y_{lh}(t) = \max(-0.17\sin(ft + \pi), 0.35\sin(ft)), \tag{41}$$

$$y_{lk}(t) = \min(0, 0.7\sin(ft + \pi)), \tag{42}$$

$$y_{rh}(t) = \max(-0.17\sin(ft), 0.35\sin(ft + \pi)), \tag{43}$$

$$y_{rk}(t) = \min(0, 0.7\sin(ft)), \tag{44}$$

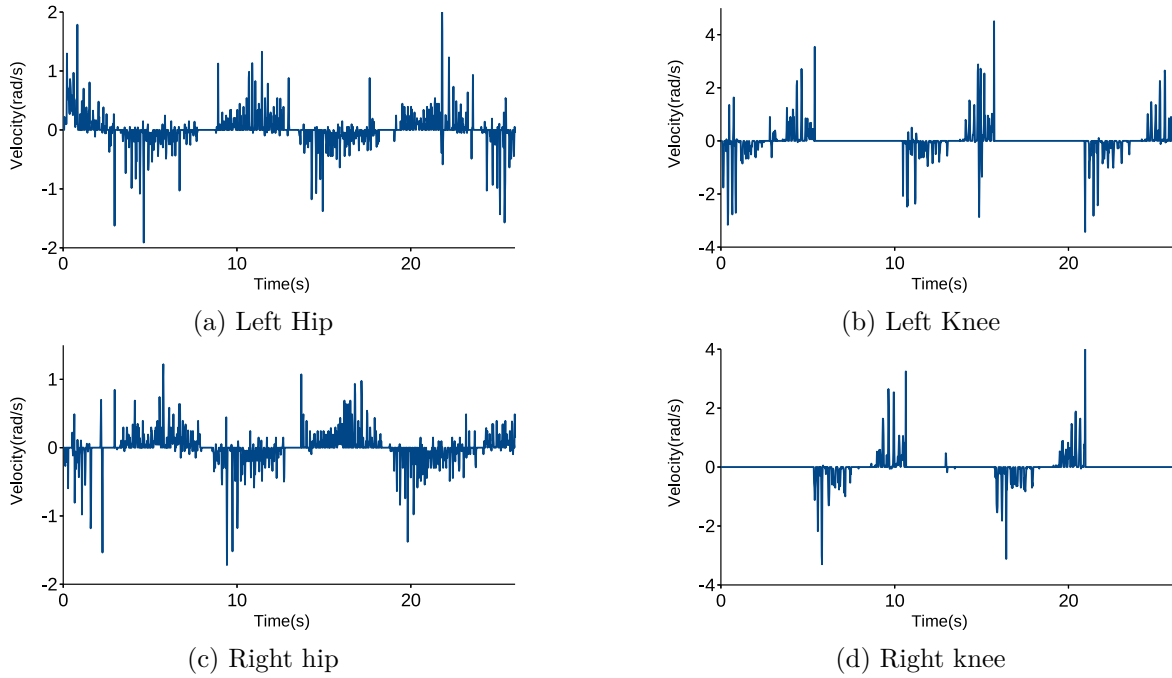
where  $t$  and  $f$  are the elapsed time and frequency.



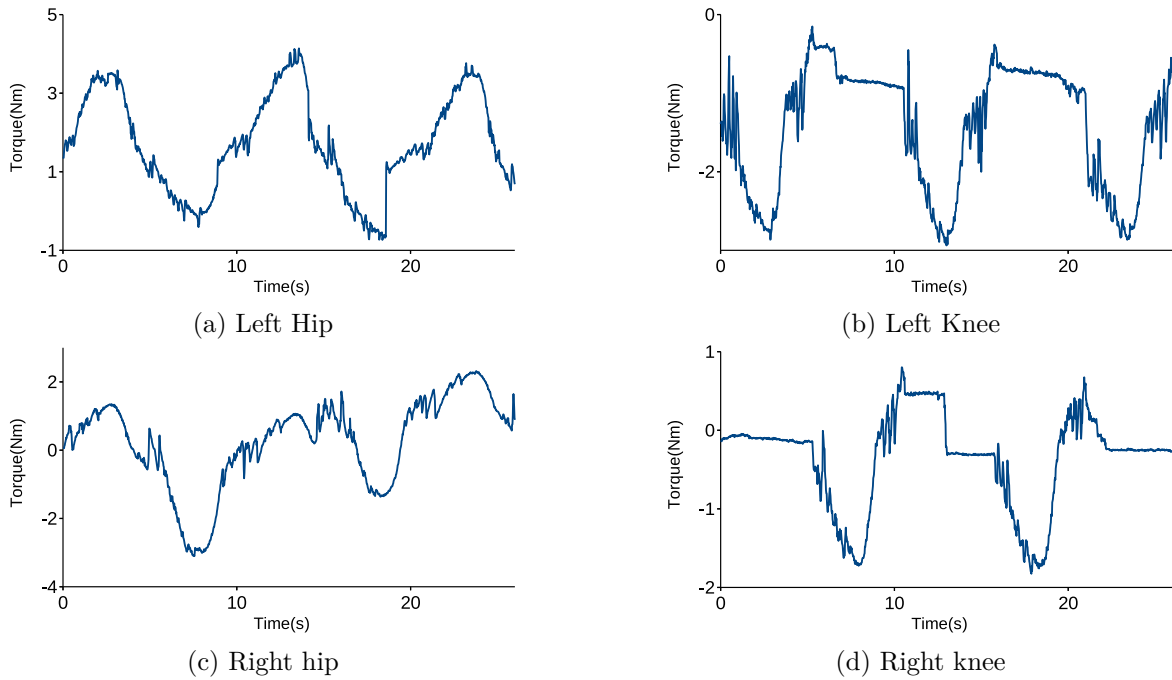
**Figure 14.** Angular trajectories of (a) left hip, (b) left knee, (c) right hip, and (d) right knee.

Figure 15 represents the angular velocity for each joint.

Figure 16 shows the torque generated by actuators of left hip, left knee, right hip, and right knee.



**Figure 15.** Angular velocity of (a) left hip, (b) left knee, (c) right hip, and (d) right knee.



**Figure 16.** Torque of (a) left hip, (b) left knee, (c) right hip, and (d) right knee.

In Figure 16, when the trajectories are in the swing phase of gait training, more torque is applied to each joint. For all joints, the maximum generated torques did not exceed the maximum torque of the DC motor, which is  $9.6Nm$ . Figure 17 illustrates the voltages applied to the hip and knee adjusted by the controller to lead each joint to pursue the desired trajectory.

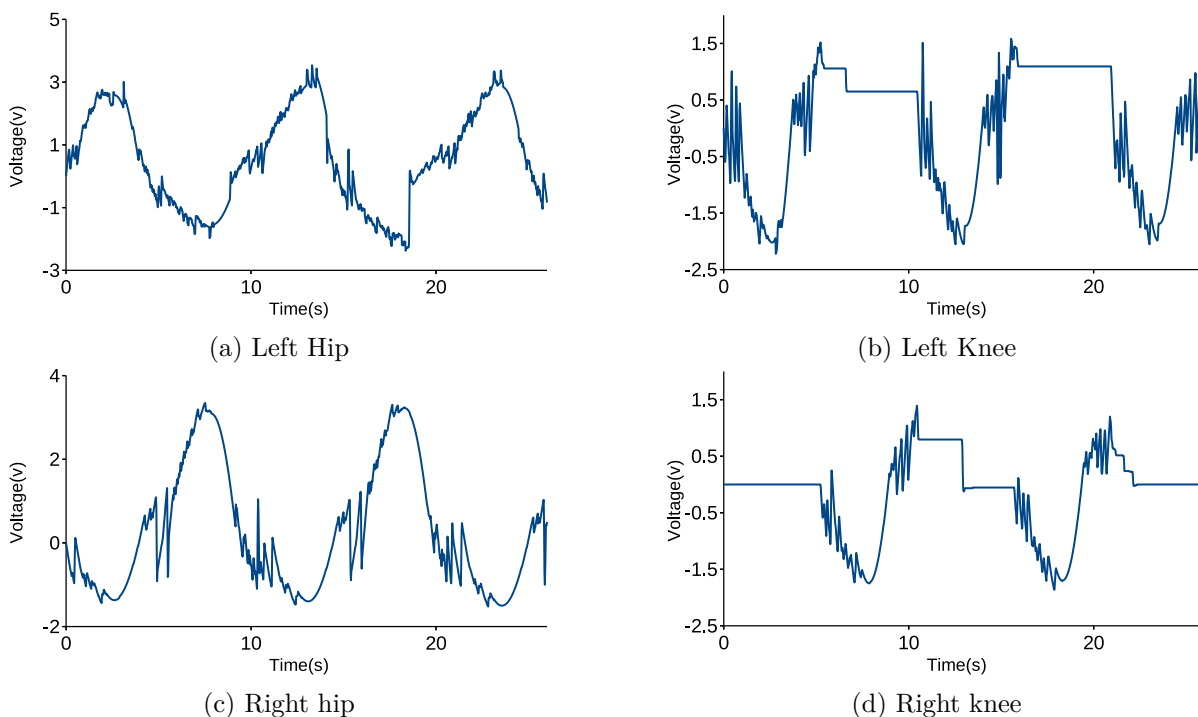


**Figure 17.** Voltage applied to (a) left hip, (b) left knee, (c) right hip, and (d) right knee.

In Figure 17, whenever the joints are in the stand phase, the controller issues the constant voltage through the actuators and while joints should follow the swing phase, the controller applies the required voltage for the actuators to produce the needed torque for each joint. Table 9 exhibits statistical analysis of error in radian for each joint, in which ME, AE, RSME, and IAE are represented.

**Table 9.** Statistical analysis of error.

Joints	Left				Right			
	ME	AE	RSME	IAE	ME	AE	RSME	IAE
Hip	0.058	0.020	0.133	0.263	0.055	0.021	0.138	0.250
Knee	0.131	0.024	0.147	0.286	0.141	0.021	0.135	0.268

AE is less than 0.05 (rad) that shows the acceptable range of error [52]. Table 10 shows the comparison of the performance of proposed ABBO and PID controller with three other works.

For the current study IAE is higher than FLC-PID demonstrated in by 97% [29] and is less than adaptive-FLC-PID given by [30] by 10 % for hip joint. However, the LLE model demonstrated in [29] and [30] are developed in Matlab/Simulink as the benchmark and they were not validated in the experimental prototype. In addition, the RMSE obtained in our work is 17% and 69% lower than PSO-PID represented in [28]. The

**Table 10.** Comparison of proposed ABBO and PID controller with others in the literature.

Approach name	Current study	PSO-PID [28]	DFA and FLC-PID [29]	adaptive-FLC-PID [30]
Type of tuning	ABBO	PSO	DFA	PSO
System model	4-DoF LLE	2-DoF LLE	4-DoF LLE	2-DoF LLE
Population size	40	20	N/A	20
No. of iteration	400	100	N/A	200
No. of design variables	4	3	N/A	3
IAE (rad)	0.263 (left hip)	N/A	0.0063 (left hip)	0.299 (hip)
	0.286 (left knee)	N/A	0.01189 (left knee)	0.281 (hip)
	0.250 (right hip)	N/A	0.0.0048 (right hip)	N/A
	0.268 (right knee)	N/A	0.0108 (right knee)	N/A
RMSE (rad)	0.133 (left hip)	0.11 (hip)	N/A	N/A
	0.147 (left knee )	0.045 (knee)	N/A	N/A

actuator used in [28] is BLCD Maxon which has the higher quality and power than the motor used in the present work.

## 8. Conclusion

In this paper, a PID controller was tuned by ABBO, in which the parameters of the migration operator changed proportionally to the number of iteration. The mathematical model of the LLE was determined by Lagrangian and Kirchhoff's law and implemented in the control system. Tuning of the PID controller was established as an optimization problem based on minimizing the steady-state trajectory error and solved by ABBO. The results were compared with other conventional BBO to show their efficiency and appropriate performance. The tuned controller experimented with an actual LLE, and the results represented an acceptable range of trajectory error. The proposed optimization performed efficiently and the control system was validated for the actual LLE. However, a more robust adaptive controller can be used for avoiding the fluctuations in joints' trajectory. This study can be extended to set optimal PID parameters in real time for the LLE application.

## Acknowledgments

The authors would like to thank The National University of Malaysia (UKM) and the Ministry of Education Malaysia for financial support received under research grants ERGS/1/2012/TK01/UKM/02/2 and KK-2020-014.

## References

- [1] Aliman N, Ramli R, Haris SM. Design and development of lower limb exoskeletons: A survey. *Robotics and Autonomous Systems* 2017; 95: 102-116. doi:10.1016/j.robot.2017.05.013
- [2] Young A, Ferris D. State-of-the-art and future directions for robotic lower limb robotic exoskeletons. *IEEE Transactions on Neural Systems and Rehabilitation Engineering* 2017; 25(2): 171-182. doi: 10.1109/TNSRE.2016.2521160
- [3] Eguchi Y, Kadone H, Suzuki K. Standing Mobility Device with Passive Lower Limb Exoskeleton for Upright Locomotion. *IEEE/ASME Transactions on Mechatronics* 2018; 23 (4): 1608-1618. doi: 10.1109/TMECH.2018.2799865

- [4] Zhang R, Wang Q, Li K, He S, Qin S et al. A BCI-based environmental control system for patients with severe spinal cord injuries. *IEEE Transactions on Biomedical Engineering* 2017; 64 (8): 1959-1971. doi: 10.1109/TBME.2016.2628861
- [5] Spiess MR, Steenbrink F, Esquenazi A. Getting the Best Out of Advanced Rehabilitation Technology for the Lower Limbs: Minding Motor Learning Principles. *Physical Medicine & Rehabilitation* 2018; 10 (9):165-173. doi: 10.1016/j.pmrj.2018.06.007
- [6] Kim KJ, Kim KH . Progressive treadmill cognitive dual-task gait training on the gait ability in patients with chronic stroke. *Journal of Exercise Rehabilitation* 2018; 14 (5): 821-828. doi: 10.12965/jer.1836370.185
- [7] Florez JM, Shah M, Moraud EM, Wurth S, Baud L et al. Rehabilitative soft exoskeleton for rodents. *IEEE Transactions on Neural Systems and Rehabilitation Engineering* 2017; 25 (2): 107-118. doi: 10.1016/j.pmr.2018.12.012
- [8] Esquenazi A, Talaty M, Jayaraman A. Powered exoskeletons for walking assistance in persons with central nervous system injuries: A narrative review. *Physical Medicine & Rehabilitation* 2017; 9 (1): 6-62. doi: 10.1016/j.pmrj.2016.07.534
- [9] Zhang T, Tran M, Huang H. Nrel-exo: A 4-DoFs wearable hip exoskeleton for walking and balance assistance in locomotion. *IEEE/RSJ International Conference on Intelligent Robots and Systems*; Vancouver, BC, Canada; 2017. pp. 508-513. doi: 10.1109/IROS.2017.8202201
- [10] Huang R, Peng Z, Cheng H, Hu J, Qiu J et al. Learning-based walking assistance control strategy for a lower limb exoskeleton with hemiplegia patients. *IEEE International Conference on Intelligent Robots and Systems*; Madrid, Spain; 2018. pp. 2280-2285. doi: 10.1109/IROS.2018.8594464
- [11] Yang Y, Huang D, Dong X. Enhanced Neural Network Control of Lower Limb Rehabilitation Exoskeleton by Add-on Repetitive Learning. *Neurocomputing* 2018; 323 (6): 256-265. doi: 10.1016/j.neucom.2018.09.085
- [12] He W, Ge SS, Li Y, Chew E, Ng YS. Neural network control of a rehabilitation robot by state and output feedback. *Journal of Intelligent & Robotic Systems* 2015; 80 (1): 15-31. doi:10.1007/s10846-014-0150-6
- [13] Shan H, Jiang C , Mao Y, Wang X. Design and control of a wearable active knee orthosis for walking assistance. *IEEE 14th International Workshop on Advanced Motion Control, AMC*; Auckland, New Zealand; 2016. pp. 51-56. doi: 10.1109/AMC.2016.7496327
- [14] Zhang Q, Zhang X, Yin G, Yang K, Xie J et al. Design on subsection based mix position controller for lower limb rehabilitation robot. *14th International Conference on Ubiquitous Robots and Ambient Intelligence, URAI*: Jeju, Korea (South); 2017. pp. 720-724. doi: 10.1109/URAI.2017.7992809
- [15] Li Z, Dong W, Wang L, Wang CCJ, Du Z. Lower limb exoskeleton hybrid phase control based on fuzzy gain sliding mode controller. *2nd International Conference on Robotics and Automation Sciences, ICRAS*; Wuhan, China; 2018. pp. 184-190. doi: 10.1109/ICRAS.2018.8442396
- [16] Simon D. Biogeography-based optimization. *IEEE Transactions on Evolutionary Computation* 2008; 12(6): 702-713. doi: 10.1109/TEVC.2008.919004
- [17] Chena X, Tianfieldb H, Duc W, Liua G. Biogeography-based optimization with covariance matrix based migration. *Applied Soft Computing Journal* 2016; 71-85. doi: 10.1016/j.asoc.2016.04.022
- [18] Paslar S, Ariffin MK, Tamjidy M, Hong TS. Biogeography-based optimisation for flexible manufacturing system scheduling problem. *International Journal of Production Research* 2014; 53 (9): 2690-2706. doi: 10.1080/00207543.2014.975855
- [19] Wen S, Chen J, Li Y, Shi D, Duan X. Enhancing the performance of biogeography-based optimization using multitopology and quantitative orthogonal learning. *Mathematical Problems in Engineering* 2017. doi: 10.1155/2017/2314927
- [20] Garg H. An efficient biogeography based optimization algorithm for solving reliability optimization problems. *Mathematical Problems in Engineering* 2015; 24: 1-10. doi: 10.1016/j.swevo.2015.05.001

- [21] Reihanian A, Feizi-Derakhshi MR, Aghdasi HS. NBBO: A new variant of biogeography-based optimization with a novel framework and a two-phase migration operator. *Information Sciences* 2019; 504: 178-201. doi: 10.1016/j.ins.2019.07.054
- [22] Misaghi M, Yaghoobi M. Improved invasive weed optimization algorithm (IWO) based on chaos theory for optimal design of PID controller. *Journal of Computational Design and Engineering* 2019; 6 (3): 284-295. doi: 10.1016/j.jcde.2019.01.001
- [23] Pal D, Chatterjee A, Rakshit A. Robust-stable quadratic-optimal fuzzy-PDC controllers for systems with parametric uncertainties: A PSO based approach. *Engineering Applications of Artificial Intelligence* 2018; 70: 38-51. doi: 10.1016/j.engappai.2018.01.003
- [24] Wang C, Fang H, He S. Adaptive optimal controller design for a class of LDI-based neural network systems with input time-delays. *Neurocomputing* 2020; 385: 292-299. doi: 10.1016/j.neucom.2019.12.084
- [25] Han S, Haoping W, Yang T. Model-free based adaptive nonsingular fast terminal sliding mode control with time-delay estimation for a 12 DOF multi-functional lower limb exoskeleton. *Advances in Engineering Software* 2018; 119: 38 -42. doi: 10.1016/j.advengsoft.2018.01.004
- [26] Li Z, Zhao K, Zhang L, Wu X, Zhang T et al. Human-in-the-Loop Control of a Wearable Lower Limb Exoskeleton for Stable Dynamic Walking. *IEEE/ASME Transactions on Mechatronics* 2021;26 (5): 2700-2711. doi: 10.1109/TMECH.2020.3044289
- [27] Sun W, Lin JW, Su SF, Wang N, Er MJ. Reduced Adaptive Fuzzy Decoupling Control for Lower Limb Exoskeleton. *IEEE Transactions on Cybernetics* 2021; 51 (3): 1099–1109. doi: 10.1109/TCYB.2020.2972582
- [28] Belkadi A, Oulhadj H, Touati Y, Khan AS, Daachi B. On the robust PID adaptive controller for exoskeletons: A particle swarm optimization based approach. *Applied Soft Computing Journal* 2017; 60: 87-100. doi: 10.1016/j.asoc.2017.06.012
- [29] Sharma R, Gaur P, Bhatt S, Joshi D. Optimal fuzzy logic-based control strategy for lower limb rehabilitation exoskeleton. *Applied Soft Computing* 2021; 105: 107226. doi: 10.1016/j.asoc.2021.107226
- [30] Aliman N, Ramli R, Haris SM, Amiri MS, Van M. A robust adaptive-fuzzy-proportional-derivative controller for a rehabilitation lower limb exoskeleton". *Engineering Science and Technology, an International Journal* 2022; 35: 101097. doi: 10.1016/j.jestch.2022.101097
- [31] Amiri MS, Ramli R, Tarmizi MAA, Ibrahim MF, Narooei KD. Simulation and Control of a Six Degree of Freedom Lower limb Exoskeleton. *Jurnal Kejuruteraan* 2020; 32 (2): 197–204. doi: 10.17576/jkukm-2020-32(2)-03
- [32] Amiri MS, Ramli R, Ibrahim MF. Hybrid design of PID controller for four DoF lower limb exoskeleton. *Applied Mathematical Modelling* 2019; 72: 17–27. doi: 10.1016/j.apm.2019.03.002
- [33] Xinyi Z, Haoping W, Yang T, Zefeng W, Laurent P. Modeling, simulation and control of human lower extremity exoskeleton. *34th Chinese Control Conference (CCC)*; Hangzhou, China ; 2015. pp. 6066–6071. doi: 10.1109/ChiCC.2015.7260588
- [34] Amiri MS, Ibrahim MF, Ramli R. Optimal parameter estimation for a dc motor using genetic algorithm. *International Journal of Power Electronics and Drive System (IJPEDS)* 2020; 11 (2): 1047–1054. doi: 10.11591/ijped.v11.i2.pp1047-1054 2020.
- [35] Dorf RC, Robert R. *Modern Control Systems*, 13th ed, Pearson Education, Inc., 2017.
- [36] Amiri MS, Ramli R, Ibrahim MF. Initialized model reference adaptive control for lower limb exoskeleton. *IEEE Access* 2020; 7: 167210-167220. doi: 10.1109/ACCESS.2019.2954110
- [37] Amiri M S, Ramli R, Ibrahim MF. Genetically optimized parameter estimation of mathematical model for multi-joints hip–knee exoskeleton. *Robotics and Autonomous Systems* 2020; 125: 103425. doi: 10.1016/j.robot.2020.103425

- [38] Castillo-Zamora JJ, Camarillo-Gomez KA, Perez-Soto GI, Rodriguez-Resendiz J. Comparison of PD, PID and sliding-mode position controllers for v-tail quadcopter stability. *IEEE Access* 2018; 6:38086–38096. doi: 10.1109/ACCESS.2018.2851223
- [39] Amiri M S, Ramli R, Ibrahim MF, Wahab DA, Aliman N. Adaptive Particle Swarm Optimization of PID Gain Tuning for Lower-Limb Human Exoskeleton in Virtual Environment. *Mathematics* 2020; 8 (11): 2040. doi: 10.3390/math8112040
- [40] Hagglund T. Signal filtering in pid control. *IFAC Proceedings Volumes* 2012; 2 (1): 1–10. doi: 10.3182/20120328-3-it-3014.00002
- [41] Amiri MS, Ramli R. Intelligent trajectory tracking behavior of a multi-joint robotic arm via genetic–swarm optimization for the inverse kinematic solution. *Sensors* 2021; 21 (9): 3171. doi: 10.3390/s21093171
- [42] Sadeghi J, Niaki STA. Two parameter tuned multi-objective evolutionary algorithms for a bi-objective vendor managed inventory model with trapezoidal fuzzy demand. *Applied Soft Computing Journal* 2015; 30: 567–576. doi: 10.1016/j.asoc.2015.02.013
- [43] Candan G, Yazgan HR. Genetic algorithm parameter optimisation using taguchi method for a flexible manufacturing system scheduling problem. *International Journal of Production Research* 2014; 53 (3): 897–915. doi: 10.1080/00207543.2014.939244
- [44] Niu Q, Zhang H, Wang X, Li K, Irwin GW. A hybrid harmony search with arithmetic crossover operation for economic dispatch. *International Journal of Electrical Power and Energy Systems* 2014; 62: 237–257. doi: 10.1016/j.ijepes.2014.04.031
- [45] Ghosh A, Das S, Mullick SS, Mallipeddi R, Das AK. A switched parameter differential evolution with optional blending crossover for scalable numerical optimization. *Applied Soft Computing Journal* 2017; 57: 329–352. doi: 10.1016/j.asoc.2017.03.003
- [46] Sumathi S, Paneerselvam S. *Computational Intelligence Paradigms Theory and Applications*, CRC Press, 2010
- [47] Li X, Yang X. Stability analysis for nonlinear systems with state-dependent state delay. *Automatica* 2020; 112: 108674. doi: 10.1016/j.automatica.2019.108674
- [48] Liu S, Liberzon D, Zharnitsky V. Almost Lyapunov functions for nonlinear systems. *Automatica* 2020; 113: 108758. doi: 10.1016/j.automatica.2019.108758
- [49] Afaq Khan MA, Swamy MN. Modified MRAC based on Lyapunov theory for improved controller efficiency. *International Conference on Automatic Control and Dynamic Optimization Techniques*; Pune, India; 2017. pp. 989–995. doi: 10.1109/ICACDOT.2016.7877735
- [50] Valluru SK, Singh M. Performance investigations of APSO tuned linear and nonlinear PID controllers for a nonlinear dynamical system. *Journal of Electrical Systems and Information Technology* 2018; 5 (3): 442–452. doi: 10.1016/j.jesit.2018.02.001
- [51] Akhil VM, Ashmi M, Rajendrakumar PK, Sivanandan KS. Human gait recognition using hip, knee and ankle joint ratios. *IRBM* 2019; 41 (3): 133–140. doi: 10.1016/j.irbm.2019.11.001
- [52] Wu J, Gao J, Song R, Li R, Li Y et al. The design and control of a 3DOF lower limb rehabilitation robot. *Mechatronics* 2016; 33: 13–22. doi: 10.1016/j.mechatronics.2015.11.010